

MAPPING THE CMB III: COMBINED ANALYSIS OF QMAP FLIGHTS

ANGÉLICA DE OLIVEIRA-COSTA^{1,2}, MARK J. DEVLIN^{3,1}, TOM HERBIG¹, AMBER D. MILLER¹,
 C. BARTH NETTERFIELD^{4,1}, LYMAN A. PAGE¹ & MAX TEGMARK^{2,5}

¹Princeton University, Department of Physics, Jadwin Hall, Princeton, NJ 08544; angelica@ias.edu

²Institute for Advanced Study, Olden Lane, Princeton, NJ 08540

³University of Pennsylvania, Department of Physics and Astronomy, David Rittenhouse Laboratory, Philadelphia, PA 19104

⁴California Institute of Technology, MS 59-33, Pasadena, CA 91125

⁵Hubble Fellow

Submitted to ApJL August 5, 1998

ABSTRACT

We present results from the QMAP balloon experiment, which maps the Cosmic Microwave Background (CMB) and probes its angular power spectrum on degree scales. In two separate flights, data were taken in six channels at two frequency bands between 26 to 46 GHz. We describe our method for mapmaking (removal of $1/f$ -noise and scan-synchronous offsets) and power spectrum estimation, as well as the results of a joint analysis of the data from both flights. This produces a 527 square degree map of the CMB around the North Celestial Pole, allowing a wide variety of systematic cross-checks. The frequency dependence of the fluctuations is consistent with CMB and inconsistent with Galactic foreground emission. The anisotropy is measured in three multipole bands from $\ell \sim 40$ to $\ell \sim 200$, and the angular power spectrum shows a distinct rise which is consistent with the Saskatoon results.

Subject headings: cosmic microwave background – methods: data analysis

1. INTRODUCTION

The QMAP balloon experiment was designed to map the Cosmic Microwave Background (CMB) and measure the angular power spectrum on degree scales. QMAP operates in the Ka (~ 30 GHz) and Q-band (~ 40 GHz) with six detectors in two polarizations (Ka1 and Ka2; Q1 and Q2; Q3 and Q4), with angular resolution between $0^\circ.6$ and $0^\circ.9$. Data were taken during two flights in 1996, the first (hereafter FL1) in June in Palestine, Texas, and the second (hereafter FL2) in November in Ft. Sumner, New Mexico. QMAP scanned a 527 square degree region near the North Celestial Pole in a complicated criss-cross pattern which allows a number of internal checks of the integrity of the measurements and results in an interconnectedness between pixels that enables efficient $1/f$ -noise removal.

A detailed description of the design and performance of the QMAP instrument and results from the first flight are presented in Devlin *et al.* (1998, hereafter D98). QMAP calibrations and results from the second flight are presented in Herbig *et al.* (1998, hereafter H98). In this *Letter*, we present the method used to analyze the QMAP experiment (the mapmaking process and the power spectrum extraction), as well as the combined results from both flights.

2. METHOD

2.1. From Scan Pattern to Map

For each of the six channels, the QMAP raw data set consists of $M=35,318,400$ observed data points y_i which we store in an M -dimensional vector \mathbf{y} . We subdivide the mapped region into N pixels whose centers $\hat{\mathbf{r}}_i$ form a rectangular grid and let x_i denote the true sky temperature in the direction $\hat{\mathbf{r}}_i$. Grouping these pixel temperatures into

an N -dimensional map vector \mathbf{x} , we can write

$$\mathbf{y} = \mathbf{A}\mathbf{x} + \mathbf{n}, \quad (1)$$

where \mathbf{n} denotes the random instrumental noise vector of size M and \mathbf{A} is a matrix of size $M \times N$ that encodes the QMAP scan strategy. We model \mathbf{n} as a random variable with zero mean and covariance matrix given by $\mathbf{N} \equiv \langle \mathbf{n}\mathbf{n}^t \rangle$. The scan strategy matrix \mathbf{A} has $\mathbf{A}_{ij} = 1$ if the i^{th} observation points to the j^{th} pixel, 0 otherwise.

The goal is to compute a map $\tilde{\mathbf{x}}$ that estimates the true map \mathbf{x} from the raw data \mathbf{y} . We use a linear method

$$\tilde{\mathbf{x}} = \mathbf{W}\mathbf{y}, \quad (2)$$

specified by some $N \times M$ matrix \mathbf{W} . Substituting (1) into (2) shows that the error in the recovered map is

$$\boldsymbol{\varepsilon} \equiv \tilde{\mathbf{x}} - \mathbf{x} = [\mathbf{W}\mathbf{A} - \mathbf{I}]\mathbf{x} + \mathbf{W}\mathbf{n}, \quad (3)$$

where \mathbf{I} is the identity matrix. Choosing \mathbf{W} to be (Tegmark 1997a, hereafter T97a)

$$\mathbf{W} = [\mathbf{A}^t\mathbf{M}^{-1}\mathbf{A}]^{-1}\mathbf{A}^t\mathbf{M}^{-1} \quad (4)$$

for some $M \times M$ matrix \mathbf{M} gives $\mathbf{W}\mathbf{A} = \mathbf{I}$, so that $\tilde{\mathbf{x}} = \mathbf{x} + \mathbf{n}$ can be interpreted as an honest-to-goodness map where the pixel noise $\boldsymbol{\varepsilon} = \mathbf{W}\mathbf{n}$ is independent of \mathbf{x} . The noise covariance matrix of the map is simply

$$\boldsymbol{\Sigma} \equiv \langle \boldsymbol{\varepsilon}\boldsymbol{\varepsilon}^t \rangle = \mathbf{W}\mathbf{N}\mathbf{W}^t. \quad (5)$$

2.2. Pre-whitening & Pink Noise Removal

Ideally, we would like to use the minimum-variance mapmaking method (Wright 1996; T97a), which corresponds to the choice $\mathbf{M} = \mathbf{N}^{-1}$. In our case, the huge matrix \mathbf{N}

is far from diagonal, since long-term $1/f$ drifts (so-called pink noise) introduce strong correlations between the noise n_i at different times. In other words, although direct application of equations (2) and (5) with $\mathbf{M} = \mathbf{N}^{-1}$ would give what we need in principle, inverting the non-sparse matrix \mathbf{N} would require a Hubble time in practice.

Fortunately, we can obtain virtually the same answer by employing a series of numerical methods detailed in Tegmark (1997b, hereafter T97b). Since the statistical properties of the noise are virtually constant in time, *i.e.*, \mathbf{N} is almost a circulant matrix¹, we replace the raw data \mathbf{y} by a high-pass filtered data set

$$\tilde{\mathbf{y}} \equiv \mathbf{D}\mathbf{y}, \quad (6)$$

where \mathbf{D} is another circulant matrix (a convolution filter), chosen so that both \mathbf{D} and the filtered noise covariance matrix $\tilde{\mathbf{N}} \equiv \langle \tilde{\mathbf{n}}\tilde{\mathbf{n}}^t \rangle = \mathbf{D}\mathbf{N}\mathbf{D}^t$ are band-diagonal. Wright (1996) referred to this as “pre-whitening” and chose the filter so that $\tilde{\mathbf{N}} \approx \mathbf{I}$. In our case, however, $\tilde{\mathbf{N}}$ is not quite circulant because of the omission of ~ 600 segments of calibration data (H98), but of the form $\tilde{\mathbf{N}} = \tilde{\mathbf{N}}_c + \tilde{\mathbf{N}}_s$, where $\tilde{\mathbf{N}}_c$ is circulant and the correction $\tilde{\mathbf{N}}_s$ is extremely sparse. We therefore choose $\mathbf{M} = \mathbf{N}_c^{-1}$, with $\tilde{\mathbf{y}}$ as the new data set.

Defining $\tilde{\mathbf{A}} \equiv \mathbf{D}\mathbf{A}$, we can rewrite (1) as $\tilde{\mathbf{y}} = \tilde{\mathbf{A}}\mathbf{x} + \tilde{\mathbf{n}}$, so equations (2) and (5) now give

$$\tilde{\mathbf{x}} = [\mathbf{A}^t \mathbf{D}^t \mathbf{M} \mathbf{D} \mathbf{A}]^{-1} \mathbf{A}^t \mathbf{D}^t \mathbf{M} \mathbf{D} \mathbf{y} \quad (7)$$

$$\tilde{\Sigma} = [\mathbf{A}^t \mathbf{D}^t \mathbf{M} \mathbf{D} \mathbf{A}]^{-1} [\mathbf{A}^t \mathbf{D}^t \mathbf{M} \tilde{\mathbf{N}} \mathbf{M}^t \mathbf{D} \mathbf{A}] [\mathbf{A}^t \mathbf{D}^t \mathbf{M} \mathbf{D} \mathbf{A}]^{-1} \quad (8)$$

which can be evaluated on a workstation in about 24 hours.

2.3. Offset Removal

In order to make maps from the data, we need to remove instrumental offsets that are synchronous with the chopper position. Although we find no evidence of atmospheric emission or sidelobe contamination, there is thermal emission from the instrument at the mK-level (H98). We solve for this scan-synchronous component by adding 160 “virtual pixels” \mathbf{x}_2 (corresponding to the 160 sampling positions along the scan) to the map vector \mathbf{x}_1 and widening the scan strategy matrix \mathbf{A} with an additional “1” in each row in one of 160 extra columns. This allows us to rewrite equation (1) as

$$\mathbf{y} = \mathbf{A}_1 \mathbf{x}_1 + \mathbf{A}_2 \mathbf{x}_2 = \mathbf{A} \mathbf{x} + \mathbf{n}, \quad (9)$$

where \mathbf{A}_1 and \mathbf{A}_2 are matrices of sizes $M \times N$ and $M \times 160$, respectively, so \mathbf{x} becomes a vector of dimension $N + 160$ and \mathbf{A} a matrix of size $M \times (N + 160)$. Since the scan strategy is so well interconnected, this method is able to produce an offset-free map at the cost of only a marginal increase in pixel noise. However, we do not wish to assume that the offset remains constant during the entire flight, as even a 10% variation in a 1 mK offset would cause an artificial signal comparable to the CMB. Since our offset is almost entirely localized in frequency to the first two harmonics of the scan rate (H98), we therefore combine the virtual pixel method with an extremely conservative

approach illustrated in Figure 1: we make \mathbf{D} a notch filter which annihilates all signals at these two frequencies, as well as the DC (0 Hz) component. Our filtering is thus more of a “pre-blueing” than a pre-whitening. The price we pay for this conservatism is that we lose essentially all information about the CMB dipole, which was detected.

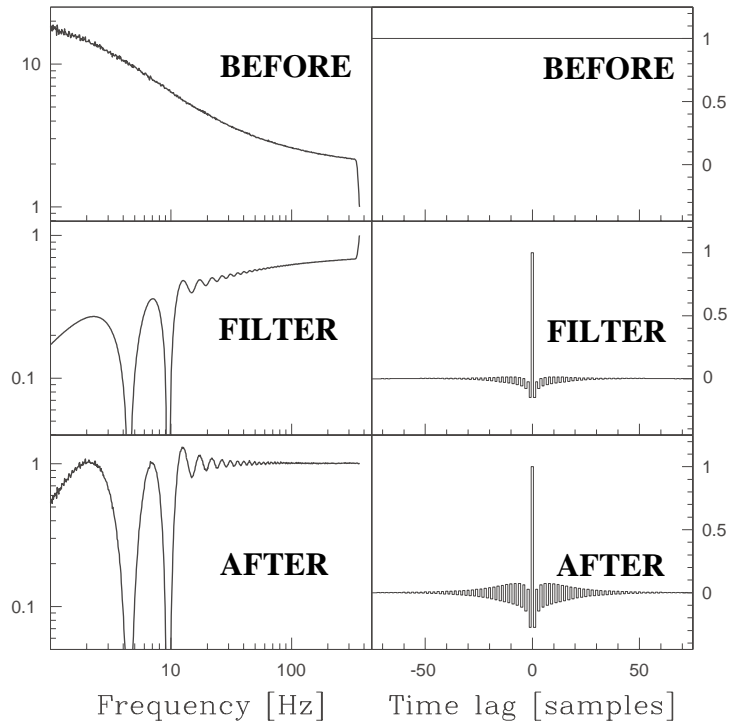


FIG. 1.— The filtering procedure is illustrated in the frequency domain (left) and in the time domain (right) for the Ka1 channel of flight 2. The noise power spectrum (top left) contains a $1/f$ -component which causes the noise to be almost perfectly correlated between measurements close together in time (top right). By multiplying the Fourier transformed signal by an appropriate filter (middle left), which corresponds to applying a convolution filter to the signal (middle right), we obtain filtered data $\tilde{\mathbf{y}}$ that has a white noise power spectrum with three “notches” (lower left), corresponding to a block-diagonal time autocorrelation function (lower right). 1 sample ≈ 1.36 ms. Vertical units are arbitrary.

2.4. Combining maps

When combining two maps \mathbf{x}_1 and \mathbf{x}_2 of the same angular resolution into a single map $\tilde{\mathbf{x}}$, we use the minimum-variance weighting

$$\tilde{\mathbf{x}} = [\tilde{\Sigma}_1^{-1} + \tilde{\Sigma}_2^{-1}]^{-1} [\tilde{\Sigma}_1^{-1} \mathbf{x}_1 + \tilde{\Sigma}_2^{-1} \mathbf{x}_2]. \quad (10)$$

The resulting covariance matrix for $\tilde{\mathbf{x}}$ is therefore

$$\tilde{\Sigma} = [\tilde{\Sigma}_1^{-1} + \tilde{\Sigma}_2^{-1}]^{-1}. \quad (11)$$

When combining maps of different resolution, the one with the higher resolution was first smoothed to the lower resolution.

¹A circulant matrix is one where each row is the previous one shifted one notch to the right. They are easily manipulated (inverted, diagonalized, *etc.*) with Fourier methods (see T97b).

2.5. Wiener-Filtered Map

In addition to the $\tilde{\mathbf{x}}$ map, we also compute the *Wiener* map \mathbf{x}_w given by (T97a)

$$\mathbf{x}_w = \mathbf{S}[\mathbf{S} + \mathbf{N}]^{-1}\tilde{\mathbf{x}}, \quad (12)$$

where $\mathbf{S} = \langle \mathbf{x}\mathbf{x}^t \rangle$ is the CMB covariance matrix, defined as

$$\mathbf{S}_{ij} = \sum_{\ell=2}^{\infty} \frac{(2\ell+1)}{4\pi} P_{\ell}(\hat{\mathbf{r}}_i \cdot \hat{\mathbf{r}}_j) B_{\ell}^2 C_{\ell}. \quad (13)$$

To avoid imprinting features on any particular scale, we use a flat fiducial power spectrum C_{ℓ} normalized to $Q = 30\mu\text{K}$, which is roughly the CMB power level we find in the maps. We approximate the QMAP beam by a circular Gaussian with FWHM values given by D98, *i.e.*, $B_{\ell} \approx e^{-\theta^2 \ell(\ell+1)/2}$ and $\theta \equiv \sqrt{8 \ln 2}$ FWHM. The Wiener filtered map \mathbf{x}_w contains the same information as $\tilde{\mathbf{x}}$, but it is more useful for visual inspection since it is less noisy.

2.6. From Map to Power Spectrum

The signal-to-noise (S/N) method (Bond 1995; Bunn and Sugiyama 1995) compresses the information content of a CMB map into a vector $\mathbf{z} \equiv \mathbf{B}^t \tilde{\mathbf{x}}$, where \mathbf{B} is an $N \times N$ matrix whose i^{th} column satisfies the generalized eigenvalue equation

$$\mathbf{S}\mathbf{b}_i = \lambda_i \mathbf{\Sigma}\mathbf{b}_i, \quad (14)$$

normalized so that $\mathbf{b}_i^t \mathbf{\Sigma}\mathbf{b}_i = 1$ and sorted by decreasing λ_i . As described in *e.g.* T97b, the N numbers z_i are uncorrelated, *i.e.*,

$$\langle z_i z_j \rangle = \mathbf{b}_i^t (\mathbf{\Sigma} + \mathbf{S}) \mathbf{b}_j = [1 + \lambda_i] \delta_{ij}, \quad (15)$$

and their variance $\langle z_i^2 \rangle$ has a contribution of 1 from noise and λ_i from signal. This means that the eigenvalue λ_i can be interpreted as a S/N ratio for z_i , and the quantities $q_i \propto (z_i^2 - 1)$ can be used as estimators of the power spectrum $\delta T_{\ell} \equiv \ell(\ell+1)C_{\ell}/2\pi$, since $\langle q_i \rangle \propto \sum_{\ell} W_{\ell} \delta T_{\ell}$ for some window function W_{ℓ} . The q_i tend to probe smaller scales as i increases and the S/N drops. The band power measurements in Table 1 and Figure 3 have been computed by normalizing the individual q_i so that their window functions integrate to unity and then averaging them in bands with a minimum-variance weighting, to minimize error bars.

3. DATA ANALYSIS

3.1. Pipeline Tests

We tested our data analysis pipeline by generating mock raw data sets that incorporate the QMAP scan strategy. These mock data sets were processed through the pipeline, recovering the original maps. When adding Monte Carlo white and pink noise to these mock data sets, we recovered maps with pixel noise consistent with the noise covariance matrix $\mathbf{\Sigma}$ computed by the pipeline. Likewise, when adding scan-synchronous offsets to these mock data sets, we recovered the original maps as well as the offsets. As expected, the original maps were faithfully recovered even when the first harmonics of these mock offsets were varied slowly throughout the flight.

We repeated our analysis for a range of pixel sizes. As expected, we found that as long as the pixels were smaller than the Shannon oversampling limit (about 2.5 times smaller than the FWHM), the maps $\tilde{\mathbf{x}}$ were virtually independent of the pixelization.

We made $\tilde{\mathbf{N}}$ as band-diagonal as possible using a filter \mathbf{D} of band width L , then neglected the tiny elements of $\tilde{\mathbf{N}}$ further than $L/2$ from the diagonal. Tests with increasing L -values showed that the results converged for $L \sim 150$, so we used $L = 320$ in the analysis to be conservative.

To test whether the Wiener maps were sensitive to our choice of power spectrum normalization, we generated Wiener maps for fiducial power spectra with $Q=20$, 30 and $40\mu\text{K}$. The visual difference between the two extreme normalizations was minimal: the maps had the same spatial features in the same locations, the $20\mu\text{K}$ map simply being slightly smoothed relative to the $40\mu\text{K}$ map.

Finally, if the beam size θ is overestimated by 1%, the band power δT_{ℓ} is overestimated by $[(\theta\ell)^2 - 2]$ percent. The first term comes from the above-mentioned Gaussian beam correction B_{ℓ} and the second from the calibration, which involves the beam area $\propto \theta^2$. Repeating our full analysis with the assumed FWHM reduced by 1σ ($\sim 3\%$), the first effect decreases the normalization of the two combined Ka band powers in Table 1 by 0.3% and 4%, respectively, whereas the second effect of course gives a 6% increase.

3.2. Data Tests

The above-mentioned scan-synchronous offset was around 1mK (FL2) and 10mK (FL1) peak-to-peak. Although our notch filter technique immunized the results towards drifts in this offset, no such drifts were actually detected.

How statistically significant is our detection of signal in the maps? Consider the null hypothesis that a map $\tilde{\mathbf{x}}$ contains merely noise, *i.e.*, $\langle \tilde{\mathbf{x}}\tilde{\mathbf{x}}^t \rangle = \mathbf{\Sigma}$. Given the alternative hypothesis $\langle \tilde{\mathbf{x}}\tilde{\mathbf{x}}^t \rangle = \mathbf{\Sigma} + \mathbf{S}$, one can show that the most powerful “null-buster” test for ruling out the null hypothesis is using the generalized χ^2 -statistic

$$\chi^2 \equiv \frac{\tilde{\mathbf{x}}^t \mathbf{\Sigma}^{-1} \mathbf{S} \mathbf{\Sigma}^{-1} \tilde{\mathbf{x}} - \text{tr} \mathbf{\Sigma}^{-1} \mathbf{S}}{[2 \text{tr} \{ \mathbf{\Sigma}^{-1} \mathbf{S} \mathbf{\Sigma}^{-1} \mathbf{S} \}]^{1/2}}, \quad (16)$$

which can be interpreted as the number of “sigmas” at which the null noise-only hypothesis is ruled out. The results of this test are given for all the individual maps in D98 and H98, and show that signal is detected at significance levels above 15σ in both flights.

Of these 11 maps (see D98 and H98), many have a substantial spatial overlap. This allows a series of powerful consistency tests, since many potential contaminants affect data from different bands and polarization channels differently. As detailed in D98 and H98, we applied the same null-buster test to the difference of the various maps in each band where they overlap spatially, and in all cases found the difference maps consistent with pure noise. Our S/N eigenmode analysis gives the same conclusion: significant signal in the best eigenmodes of the individual channels, but S/N -coefficients consistent with pure noise in the difference maps. Thus all of the significant signal appears to be common to the different channels, indicating

that the bulk of the detected signal is due to temperature fluctuations on the sky.

3.3. Foreground Contamination

To constrain the frequency dependence of our signal, we repeated the null-buster test for weighted difference maps of the form

$$\tilde{\mathbf{x}} \equiv \tilde{\mathbf{x}}_1 - (\nu_2/\nu_1)^\beta \tilde{\mathbf{x}}_2, \quad (17)$$

where the map $\tilde{\mathbf{x}}_1$ and the frequency ν_1 was for the Ka-band and $\tilde{\mathbf{x}}_2$ and ν_2 was for the Q-band. This placed a $2\text{-}\sigma$ lower limit on the spectral index β of -1.4 , which means that the signal cannot be dominated by foregrounds such as free-free emission ($\beta \sim -2.15$) or synchrotron radiation ($\beta \sim -2.8$). A more detailed foreground analysis, cross-correlating the maps with various foreground templates, will be presented in a separate paper (de Oliveira-Costa *et al.* 1998).

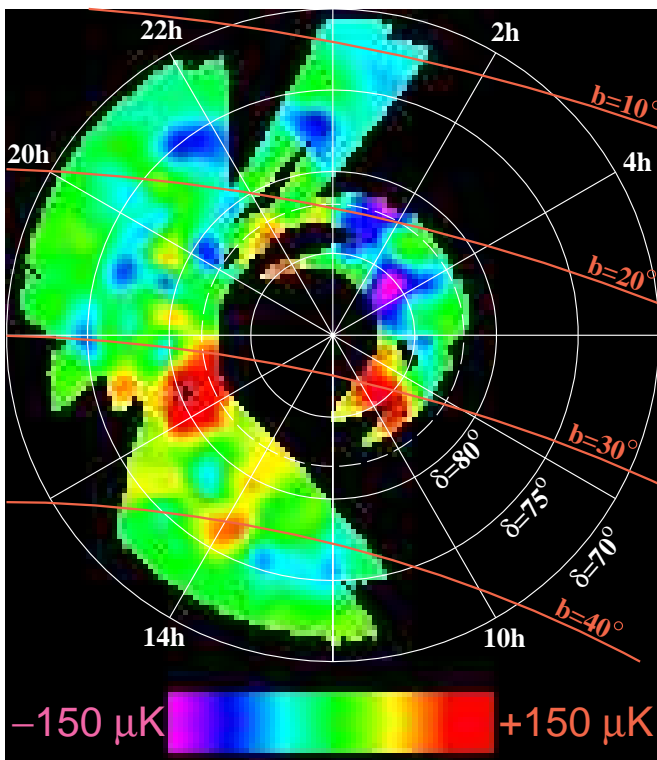


FIG. 2.— Wiener-filtered map of the QMAP combined data. The dashed circle shows the Saskatoon coverage.

4. RESULTS & CONCLUSIONS

The Wiener map obtained by combining all the data from both flights is shown in Figure 2. The above-mentioned generalized χ^2 -test shows that the signal observed in this figure is significant at the $\gtrsim 15\sigma$ -level.

This map covers 527 square degrees, and has a substantial overlap with the 200 square degree Saskatoon map. Visual comparison of the two maps in the overlap region reveals striking similarities, providing further indication

that the bulk of the detected signal is due to temperature fluctuations on the sky rather than systematic effects. A detailed statistical comparison of the QMAP and Saskatoon data sets will be presented in a future paper.

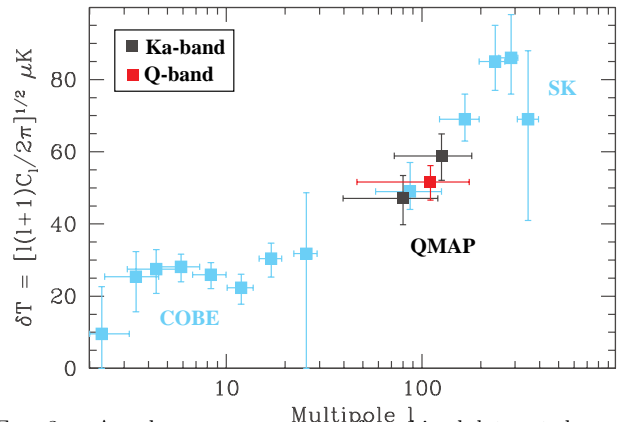


FIG. 3.— Angular power spectrum of combined data set shown in Figure 2. The results are listed in Table 1.

The power spectrum for the total data set (FL1+FL2) is given in Figure 3 and Table 1. We see that it agrees well with the Saskatoon power spectrum (Netterfield *et al.* 1997), showing a rise on degree scales to power levels substantially above those found on large scales by COBE. The calibrated raw data with pointing will be made public after publication of this *Letter*.

Table 1. — The angular power spectrum. The band powers $\delta T_\ell \equiv [\ell(\ell+1)C_\ell/2\pi]^{1/2}$ have window functions whose mean and rms width are given by ℓ_{eff} and $\Delta\ell$. The full window functions are available at <http://dept.physics.upenn.edu/cmb.html> and <http://pupgg.princeton.edu/~cmb/welcome.html>. The errors δT are uncorrelated within each pair of Ka-points. The first and second one in each pair is dominated by sample variance and detector noise, respectively. Calibration errors are not included (see H98).

Flight	Band	ℓ_{eff}	$\Delta\ell$	δT
1	Ka	92	45	49^{+6}_{-7}
	Q	84	46	47^{+8}_{-10}
2	Ka	91	47	46^{+10}_{-12}
	Ka	145	64	63^{+10}_{-12}
	Q	125	67	56^{+5}_{-6}
1+2	Ka	80	41	47^{+6}_{-7}
	Ka	126	54	59^{+6}_{-7}
	Q	111	64	52^{+5}_{-5}

We would like to thank Wayne Hu for helpful comments. This work was supported by a David & Lucile Packard Foundation Fellowship (to LP), a Cottrell Award from Research Corporation, an NSF NYI award, NSF grants PHY-9222952 and PHY-9600015, NASA grant NAG5-6034 and Hubble Fellowships HF-01044.01–93A (to TH) and HF-01084.01–96A (to MT) from by STScI, operated by AURA, Inc. under NASA contract NAS5-26555.

REFERENCES

Bond, J.R. in *Cosmology and Large Scale Structure*, 1995, p469
 Bunn, E.F., Sugiyama, N., 1995, ApJ, 446, L49-52
 de Oliveira-Costa, A., *et al.*, 1998, in preparation
 Devlin, M.J., *et al.* 1998, astro-ph/9808043 (D98)
 Herbig, T., *et al.* 1998, astro-ph/9808044 (H98)

Netterfield, C.B., *et al.*, 1997, ApJ, 474, 47-66
 Tegmark, M. 1997a, ApJ, 480, L87-90 (T97a)
 Tegmark, M. 1997b, Phys. Rev. D, 56, 4514-4529 (T97b)
 Wright, E. L. 1996, astro-ph/9612006